Journal of Alloys and Compounds 811 (2019) 152030

Contents lists available at ScienceDirect

Journal of Alloys and Compounds

journal homepage: http://www.elsevier.com/locate/jalcom

Comparative study of structure and phase transitions in Fe-(25–27)% Ga alloys

I.S. Golovin [a, *], A.K. Mohamed [a, **], V.V. Palacheva [a], V.V. Cheverikin [a], A.V. Pozdnyakov [a], V.V. Korovushkin [a], A.M. Balagurov [b, c], I.A. Bobrikov [b], N. Fazel [d], M. Mouas [d], J.-G. Gasser [d], F. Gasser [d], P. Tabary [a, e], Q. Lan [f], A. Kovacs [f], S. Ostendorp [g], R. Hubek [g], S. Divinski [g], G. Wilde [g]

[a] National University of Science and Technology "MISIS", Leninsky ave. 4, 119049, Moscow, Russia
[b] Frank Laboratory of Neutron Physics, Joint Institute for Nuclear Research, 141980, Dubna, Russia
[c] Lomonosov Moscow State University, 119991, Moscow, Russia
[d] Université de Lorraine. Laboratoire de Chimie et Physique, 1 boulevard Arago, 57078, Cedex 3, Metz, France
[e] Ecole des Mines de Saint-Etienne, 158 cours Fauriel, F-42023, Saint-Etienne, Cedex 2, France
[f] Ernst Ruska-Centre for Microscopy and Spectroscopy with Electrons, Forschungszentrum Jülich, 52425, Jülich, Germany
[g] Institute of Materials Physics, University of Munster, Wilhelm-Klemm-Str. 10, 48149, Münster, Germany

ARTICLE INFO

Article history:
Received 29 May 2019
Received in revised form
13 August 2019
Accepted 26 August 2019
Available online 29 August 2019

Keywords:
Fe-Ga
Metastable and equilibrium structure
Phase transitions
Ordering
In situ neutron diffraction
Resistivity

ABSTRACT

A wide range of complementary research technique - XRD, SEM, TEM, MFM, HV, and low temperature heat capacity, in situ neutron diffraction, resistivity, vibrating sample magnetometry, internal friction, dilatometry, and differential scanning calorimetry - is applied to study structure and phase transitions at heating and cooling of two Fe–Ga functional alloys with 25 and 27 at.% Ga. Using high resolution neutron diffraction, it is unambiguously proven that the initial state of both as-cast samples at room temperature is the D03 phase which results from ordering of the high temperature A2 phase during cooling. Heating of as-cast samples and their subsequent cooling leads to a cascade of phase transitions which change the samples' structural, mechanical and physical properties. These transitions and properties are discussed in the paper. Transition from metastable $D0_3$ to stable $L1_2$ phase at heating or isothermal annealing leads to significant changes in macro (grain size) and micro (ordering) structure, hardness and magnetic properties (magnetostriction, magnetization). According to our structural studies (ND, XRD), composition Fe-25.5 at.%Ga below ~600 °C belongs to a single phase ($L1_2$) range of the equilibrium phase diagram, while in the Fe-26.9Ga alloy some amount of the $D0_{19}$ phase is also present.

1. Introduction

Magnetostrictive materials appear poised to play an increasingly important role in applications ranging from active vibration control, control surface deployment and energy harvesting to stress and torque sensing. One of the reasons for the promise of these materials in a host of applications is the development of a new class of structural magnetostrictive materials, iron–gallium alloys (galfenol). These alloys exhibit moderate magnetostriction (~350 ppm) under very low magnetic fields 100 Oe (8000 A.m^{-1}), have very low hysteresis, and demonstrate high tensile strength (500 MPa) and limited variation in magnetomechanical properties for temperatures between −20 and 80 °C [1]. These materials are machinable, ductile and can be welded. Thus, they can be easily threaded, attached to existing structures and used as load bearing members. They have a high Curie temperature [1] and are corrosion resistant [2] and biodegradable [3]. The raw materials used to produce Fe–Ga alloys are relatively inexpensive [2]. All these factors demonstrate that Fe–Ga alloys have great promise as an engineering material for actuation and sensing applications.

The past few decades have witnessed extensive magnetostrictive materials applications in such different fields as sensors, actuators and transducers [4,5], in which alloys of giant room-

* Corresponding author. Leninsky ave. 4, 119049, Moscow, Russia.
** Corresponding author. Leninsky ave. 4, 119049, Moscow, Russia.
E-mail addresses: i.golovin@misis.ru (I.S. Golovin), abdelkarim.abdelkarim@feng.bu.edu.eg (A.K. Mohamed).

https://doi.org/10.1016/j.jallcom.2019.152030
0925-8388/

temperature magnetostriction of Terfenol-D ($Tb_{1-x}Dy_xFe_2$) have been widely used. However, Terfenol-D is limited by its mechanical brittleness, heavy use of rare earth elements, and high magnetic saturation field [6]. Galfenol ($Fe_{1-x}Ga_x$) alloys have the advantages of excellent ductility, low cost, and low magnetic saturation field [7]. Iron magnetostriction is enhanced tenfold when a fraction of its atoms is replaced by nonmagnetic Ga [8–11], although it is still much lower than that of Terfenol-D. Great efforts have been made to further improve the magnetostriction by adding 3d and 4d transition elements such as Ni, V, Cr, Mn, Co, Mo, and Rh [12–15], or interstitial elements such as C, B and N [16,17].

Further optimization of Fe–Ga alloy properties is possible if phase transitions of sequence and kinetics is completely characterized. Some calculations of phase stability were recently done in Ref. [18]. In spite of the longstanding interest to Fe–Ga alloys with attractive magnetic properties, the existing phase diagrams, both at equilibrium [19–21] and metastable [22], do not provide proper information about the structure of the alloys produced within commercially applied heat treatment regimens (cooling and heating with different rates and isothermal annealing). Usage of these simple tools allows the varying of their micro- and phase structures and, consequently, their functional properties to a large extent.

The aim of this paper is twofold: it is not only to study both the structure and sequence of phase transitions in metastable alloys (as-cast Fe-25Ga and Fe-27Ga alloys), but also to examine the rates of the transitions using different techniques, including both in situ tests with different heating rates and long-term isothermal annealing treatments. Those properties are of high interest and importance in order to design specific microstructures with desired properties.

2. Experimental procedure

This work was carried out on two alloys with nominal compositions Fe-25%Ga and Fe-27%Ga. The alloys were produced by the same manner in an Indutherm MC-20 V mini furnace by induction melting under protective high-purity argon gas. After preparation, the analysis of the chemical composition by Energy Dispersive X-ray Spectroscopy (EDX) revealed the following compositions Fe-$26.9^{\pm0.1}$at.%Ga (nominal composition Fe-27Ga) and Fe-$25.5^{\pm0.1}$at.% Ga (nominal composition Fe-25Ga). The tolerance (±0.1) comes from the calibration by measuring standard samples with a purity of 99.9999% of element. The standard error of measurement of the chemical composition is 0.1–0.2% wt. In this paper we use only atomic %.

Neutron diffraction (ND) patterns were measured with a high-resolution Fourier diffractometer (HRFD) operating at the IBR-2 pulsed reactor at JINR (Dubna, Russia). The HRFD can be switched between high-resolution ($\Delta d/d \approx 0.0015$) and high-intensity ($\Delta d/d \approx 0.015$) diffraction modes, both of which are needed for a joint analysis of the changes in the atomic structure and microstructure of the material upon heating or cooling. A detailed description of the method is given in Ref. [23], where a comparative analysis of the results obtained on as-cast and powder samples of the Fe-27Ga alloy was carried out. Most of the in situ experiments were carried out with heating and cooling rates of 2 °C/min. Some tests were also carried out with a heating rate of 20 °C/min and cooling rates of 1, 4, 8 °C/min, respectively.

X-ray diffraction (XRD) analysis of the crystallographic structure of the samples were performed with a Bruker D8 Advanced diffractometer with Cu K_α radiation. The room temperature XRD tests and selected SEM-EBSD tests we used after 300 h annealing in vacuum at different temperatures, namely: 300 °C, 350 °C, 400 °C, 450 °C, 500 °C, 575 °C, respectively.

Mössbauer spectroscopy was carried out on spectrometer Ms-1104 Em at room temperature using γ-source ^{57}Co and powdered samples. Isomeric (chemical) shift determined relative to α-Fe.

Resistivity measurements (RM) The resistivity is measured by the so-called four-probe technique during heating and cooling rate of 1 °C/min. Experimentally we use a LabView program designed by F. Gasser, and an experimental device described by Abadlia et al. [24] and more recently by Messaoud et al. [25]. The relative accuracy can be better than 0.1% and the resolution reaches 0.01%. This technique is very sensitive, measuring very small resistivity variations to microstructure details including defects, ordering, and presence of impurities.

Internal friction (IF), or the loss factor Q^{-1}, were obtained from forced vibrations by measuring the phase lag tanφ between the applied cyclic stress and the resulting strain: $\sigma = \sigma_0 \cos(\omega t)$ and $\varepsilon = \varepsilon_0 \cos(\omega t + \varphi)$, correspondingly. $\omega = 2\pi f$ and φ is the phase lag or the loss angle [26]. The temperature-dependent measurements were conducted as a function of temperature between 0 and 600 °C using forced bending single cantilever vibrations with $\varepsilon_0 = 7 \times 10^{-5}$ with heating and cooling rates of 2 °C/min.

Differential scanning calorimetry (DSC) experiments using a Labsys Setaram system with heating rates of 5, 10 and 20 °C/min in air atmosphere allowed us to carry out the sample's thermal analysis.

Low-temperature heat capacity was measured using a physical property measurement setup (PPMS by Quantum Design) in the temperature interval from about 2 to 100 K for alloys and from 2 to 400 K for pure reference metals (Fe and Ni). After cooling and equilibration at about 2 K, single heat pulses are applied to the sample and its temperature response is measured. The so-called two-tau method [27] was followed. A special low-temperature grease was applied to the heating stage to guarantee a good thermal contact. The specific heat capacities of the systems "heating stage + grease + sample" and of "heating stage + grease" were measured separately. Further details are identical to those in Ref. [28].

The dilatometry tests (DT) were recorded at temperatures ranging from 20 °C to 800 °C at the heating rate of 5 °C/min using a Dilatometer Linseis L75.

Magnetization (VSM) curves were obtained using a VSM-130 vibrating sample magnetometer with a heating rate of 6 °C/min under a magnetic field of ≈400 kA/m.

SEM-EBSD microstructures of the alloys were identified by scanning electron microscopy (SEM) operating at 20 kV using a TESCAN VEGA LMH microscope with a LaB6 cathode and an energy dispersive X-ray microanalysis system (Oxford Instruments, Software Advanced AZtecEnergy). Both backscattered electron and secondary electron imaging were used in the analysis. Electron backscatter diffraction (EBSD) analysis of the alloys was investigated using the NordlysMax2 detector (Oxford Instruments, Software Advanced AZtecEnergy) with a Crystal Structure Database supplied by Oxford Instruments. The mean angular deviation (MAD) of 0.25 was used in the analysis.

TEM: Electron transparent specimens for transmission electron microscopy (TEM) were prepared using focused Ga ion beam sputtering in a scanning electron microscope (ThermoFisher Helios 440). The ion energies were gradually decreased from 30 kV to 5 kV as the specimen thickness approached ~100 nm. The TEM specimen was attached to a copper Omniprobe grid regularly used for lift-out specimen preparation. The surface damage was reduced by low-energy focused Ar ion milling at 0.9 kV ion energy (Fischione Nanomill). Bright-field (BF) TEM images and selected area electron diffraction (SAED) patterns were recorded using a charge couple device (CCD) camera in a field emission transmission electron microscope operated at 200 kV (ThermoFisher Tecnai G2).

MFM: A Dual Scope C26 magnetic force microscope, MFM (DME

Company, Copenhagen, Denmark) was used to obtain the magnetic force gradient image with a typical lift height of 250 nm and a high moment Co-coated tip magnetized normal to the sample surface. The MFM facility used for this study is equipped with an optical microscope with a magnification of 300×.

Hardness (HV) of the alloys was measured with a micro-indentation Vickers tester 402-MVD WOLPERT with a dwell time of 15 s and a load of 100 g. For the HV tests we used the samples after 300 h annealing in vacuum at different temperatures, namely: 300, 400, 500 °C.

Heating rates and atmospheres used in the experiments are summarized in Table 1.

3. Results and discussion

3.1. As-cast state of alloys

According to the phase diagram proposed by Köster et al. [19–21] and Kubashevski [29] the equilibrium structure of Fe-26.9Ga and Fe-25.5Ga alloys at room temperature (RT) must be 100%$L1_2$ phase and about 90%$L1_2$ + 10%A2 phase respectively (Fig. 1). In contrast to the equilibrium diagram, the as-cast alloys exhibit a $D0_3$ ordered structure with lattice parameters 5.8130 and 5.8172 Å, correspondingly (Fig. 2 a, b). These results are in agreement with our previous estimations of structure and lattice parameters [30].

From the analysis of the diffraction peak widths, it may be concluded that the initial state of both samples consists of domains of about 1400–1800 Å in size with long-range ordered $D0_3$ structure. This statement is supported by the data presented in Fig. 3, where one can see that the widths of all diffraction peaks (fundamental and superstructure) for both samples can be fitted by a single dependence on d-spacings. Details of the Williamson-Hall analysis can be found in Ref. [23].

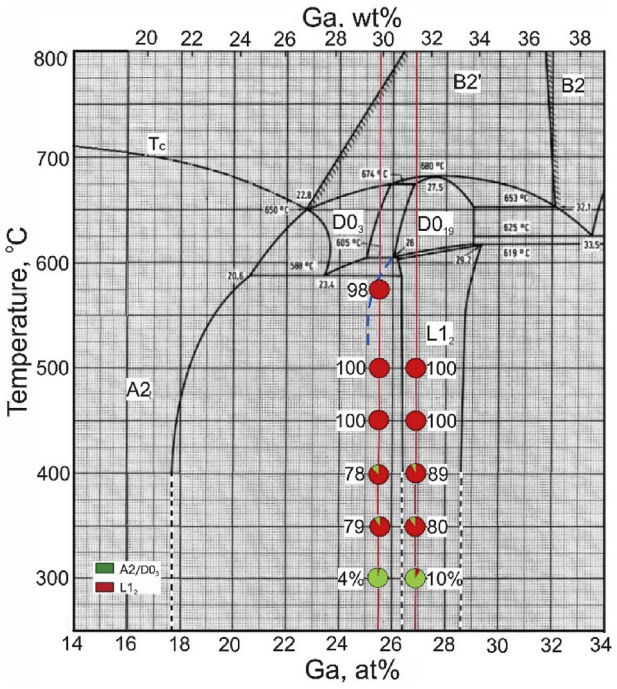

Fig. 1. Equilibrium phase diagram Fe-Ga [19–21] with two vertical red lines corresponding to the studied compositions. Green/red circles indicate alloy structure after 300 h annealing at indicated temperatures. Red and green colors correspond to EBSD colors in Fig. 4: green shows volume fraction of BCC derivative $D0_3$ phase; red reveals – FCC derivative $L1_2$ phase. (For interpretation of the references to color in this figure legend, the reader is referred to the Web version of this article.)

3.2. Phase transitions during heating

Three disordered (A1, A2, A3) and four ordered (B2, $D0_3$, $L1_2$, $D0_{19}$) phases were observed in this study at different temperatures either by in situ neutron diffraction tests or after long-term annealing by XRD:

1. A1 with γ-Fe-type structure with Fe and Ga atoms randomly distributed, sp.gr. *Fm*3*m*;
2. A2 with α-Fe-type structure with Fe and Ga atoms randomly distributed, sp. gr. Im3*m*;
3. A3 with hexagonal close packed disordered structure, sp.gr. $P6_3/mmc$;
4. B2 with a CsCl-type structure with Fe and Ga atoms partially ordered, sp. gr. *Pm*3 *m*, $a_{B2} \approx a_{A2}$;
5. $D0_3$ with a BiF_3-type structure with Fe and Ga atoms partially ordered, sp. gr. *Fm*3*m*, $a_{D03} \approx 2a_{A2}$;
6. $L1_2$ with a Cu_3Au-type structure with Fe and Ga atoms partially ordered, sp. gr. *Pm*3 *m*, $a_{L12} \approx a_{A1}$;
7. $D0_{19}$ with a $MgCd_3$-type structure with Fe and Ga atoms partially ordered, sp. gr. $P6_3/mmc$, $a_{D019} \approx 2a_{A3}$, $c_{D019} \approx c_{A3}$.

3.2.1. In situ neutron diffraction

In situ neutron diffraction studies were carried out with heating rates of 2 °C/min for both alloys proving the following phase transitions:

- **for Fe-25.5Ga** and heating rate of 2 °C/min: $D0_3 \rightarrow L1_2 \rightarrow D0_{19} \rightarrow (A2 + B2) \rightarrow A2$ in contrast with the cascade of transitions suggested by the equilibrium phase diagram: $D0_3 \rightarrow (L1_2 + D0_3) \rightarrow (D0_{19} + D0_3) \rightarrow B2 \rightarrow A2$. This difference is discussed below. The partially ordered B2 phase appearing shortly in the (700–750)°C temperature range occupies not more than 30% of the sample volume, i.e. it coexists with the disordered A2 phase.
- **for Fe-26.9Ga** and a heating rate of 2 °C/min: $D0_3 \rightarrow L1_2 \rightarrow D0_{19} \rightarrow (A2 + B2) \rightarrow A2$ in full agreement with existing phase diagrams. In the case of a heating rate of 20 °C/min, the B2 phase

Table 1
Test conditions: heating rate, atmosphere, highest temperature.

	In situ tests						*Tests at RT*		
	RM	ND	TDIF	DT	VSM	DSC	XRD	EBSD	HV
Heating rate, °C/min	1	2	2	5	6	5, 10, 20	RT	RT	RT
Atmosphere	Argon	Vacuum	air	air	air	air	vacuum	vacuum	air
End T, °C	1000	800	600	800	750	800	RT	RT	RT

RT – room temperature tests after 300 h annealing of the samples at different temperatures.

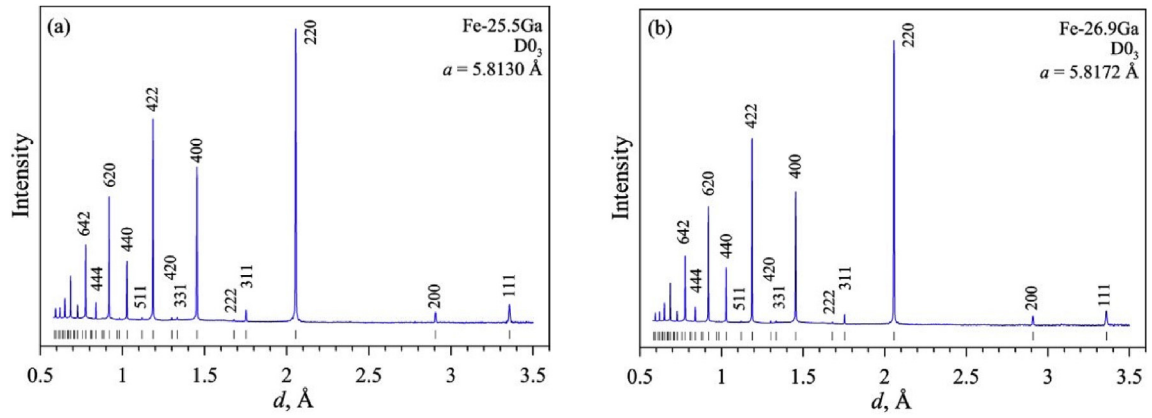

Fig. 2. High-resolution neutron diffraction patterns of the Fe-25.5Ga (a = 5.8130 Å) (a) and Fe-26.9Ga (a = 5.8172 Å) (b) alloys measured in their initial state (before heating). Both samples are in the $D0_3$ phase. Miller indices of several first peaks are specified, the vertical bars indicating the calculated peak positions.

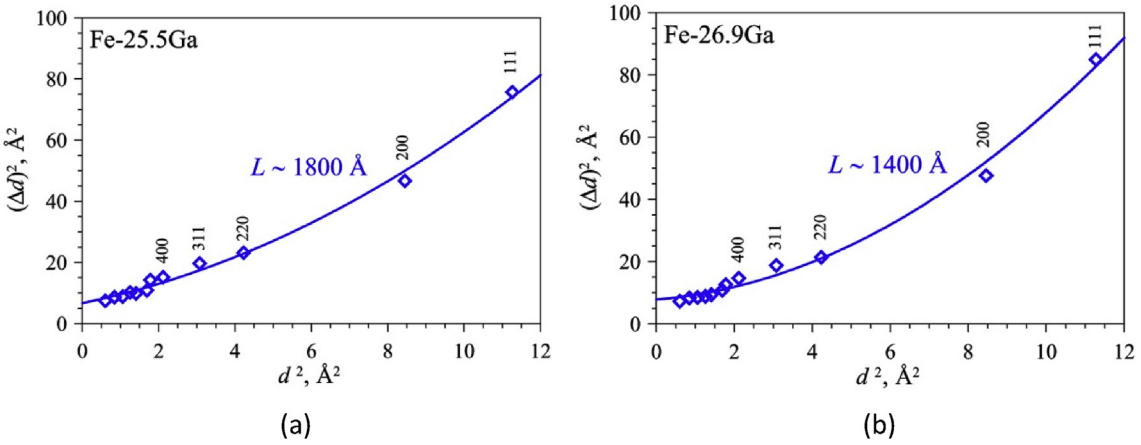

Fig. 3. The $(\Delta d)^2$ over d^2 dependences (Williamson-Hall plots) for Fe-25.5Ga (a) and Fe-26.9Ga (b) samples in the as-cast state. The $(\Delta d)^2$ values are multiplied by 10^6. The statistical errors of the experimental points are about the symbol size. The coherently scattering domain size (L) and the Miller indices of several first peaks are pointed out.

was indistinguishable and instead of the $D0_{19} \rightarrow B2 \rightarrow A2$ reaction we recorded only the $D0_{19} \rightarrow A2$ transition;

In situ neutron diffraction measurements performed with a heating rate of 2 °C/min show some similarities of the phase transitions for the two studied alloys at temperatures below ~600 °C, but with some differences at higher temperatures (Fig. 4 a, b).

At room temperature the Fe-25.5Ga sample (a) is in the $D0_3$ state, which is characterized by the 111, 200, and 311 superstructure diffraction lines. After that the phases $L1_2$ (100 and 110 lines), $D0_{19}$ (100 and 101 lines), B2 (100 line), and A2 appear. At cooling, the process occurs in the opposite direction (without the formation of the $D0_{19}$ phase) with the appearance of a stable phase $L1_2$. At room temperature the Fe-26.9Ga sample (b) is in the $D0_3$ state, which is characterized by the 111, 200, and 311 superstructure diffraction lines. The subsequent phases $L1_2$ (100 and 110 lines), $D0_{19}$ (100 and 101 lines), B2 (100 line) and A2 appear. During cooling, the process proceeds in the opposite direction with the appearance of a mixed state $D0_{19} + L1_2$ below 500°C.

These results with the corresponding temperature intervals of the phase transitions are shown in Fig. 5 a and b for Fe-25.5Ga and Fe-26,9Ga, respectively. The lattice parameters for different phases as a function of temperature for similar alloys can be seen in Ref. [23].

3.2.2. Electrical-resistivity

To the best of our knowledge, this method is used for the first time to characterize phase transitions in Fe—Ga. The resistivity is, in some sense, similar to X-ray and neutron diffraction: in these three techniques, the particles (X-rays, neutrons and free electrons inside the metal) are scattered by different potentials. Only the electrons at the Fermi level may be scattered and contribute to the resistivity. X-rays examine the surface while neutrons and electrons study the bulk. Like neutrons, electrons also react to the magnetism of the metals. The Curie point corresponds to a change of the slope of the resistivity versus temperature, (see the paper of Abadlia et al. [24]). Resistivity and DSC give the same physical information when the heating rate is the same. However, resistivity measurements offer advantages for measurements at low rates, since the signal magnitude does not depend on the heating or cooling rate. In fact, resistivity measurements continue to give information even if the temperature does not change any further, e.g. for ageing at constant temperature.

As can be seen in Fig. 6, we observe a first change of the slope at 399 °C, then a second at 430 °C (±2 °C). The resistivity increases continuously from 430 °C and its increase ends at 485 °C considering the derivative curve. This is coherent with the $D0_3$ to $L1_2$ transition observed in Fig. 5. The derivative curve maximum is at 462 °C. At 615 °C we observe the onset of a new phase transition.

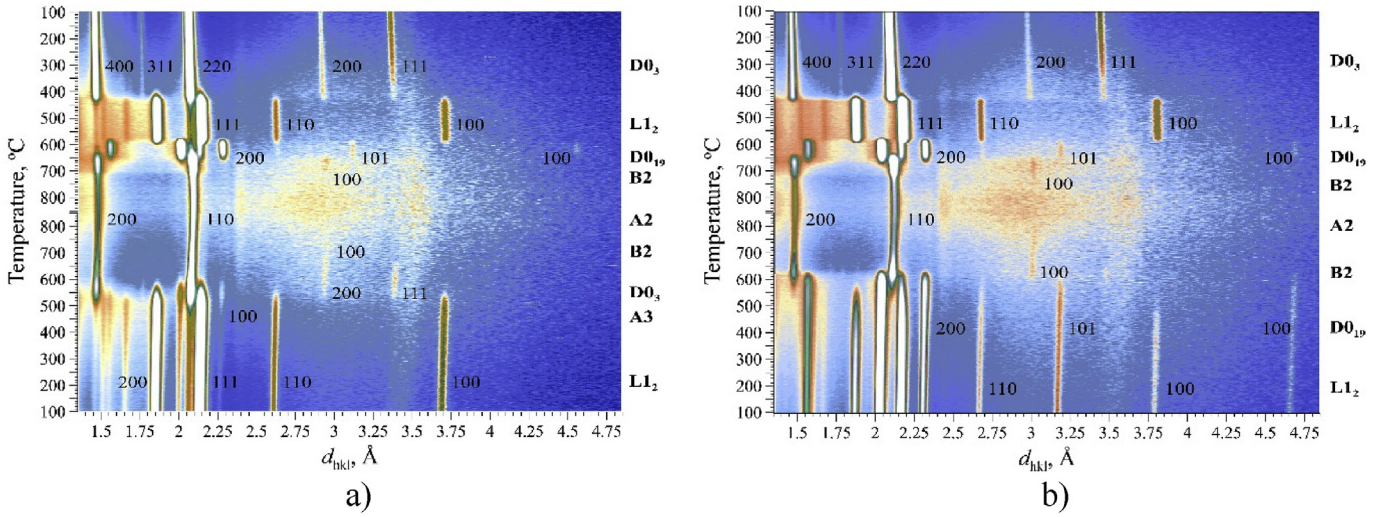

Fig. 4. A 2D visualization of the diffraction pattern evolution of the Fe–25.5Ga (a) and Fe–26.9Ga (b) samples in the as-cast state measured upon slow heating up to 850°C and subsequent cooling down in the real-time mode. The temperature (and time) axis goes from top to bottom; *d*-spacing axis goes from left to right.

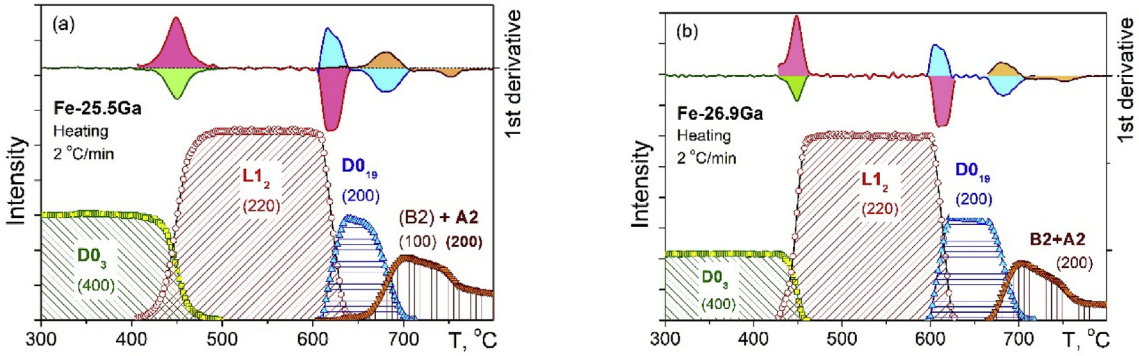

Fig. 5. Temperature dependences of the intensities of the fundamental diffraction peaks and their first derivatives (transformation rate, right upper Y-axe) of different phases during the transition from the initial ($D0_3$ phase at RT) to the final (A2 phase above 750 °C) state of the alloy Fe-25.5Ga (a), and of the alloy Fe-26.9Ga as well (b) during heating.

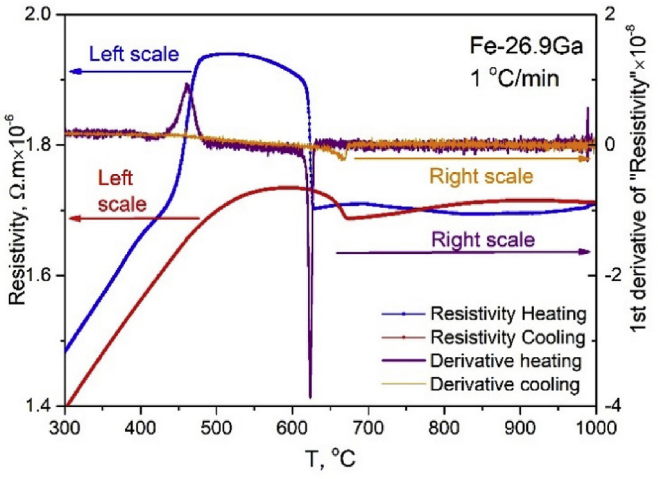

Fig. 6. Temperature dependence of the resistivity (during heating and cooling) and its first derivative for the as-cast Fe-26.9Ga alloy.

The maximum is reached at 624 °C and ends at 628 °C. The change, which begins at 615 °C and ends at 628 °C, can be compared to the $L1_2$ to $D0_{19}$ transition near 610 °C on the equilibrium phase diagram and on Fig. 5. Above 628 °C the next change of the slope is observed at 693 °C, where it can be associated with the $D0_{19}$ to B2 transition temperature of 678 °C in the phase diagram. The change of slope at 825 °C corresponds to the B2 to A2 phase transformation.

3.2.3. *Vibrating sample magnetometry*

The magnetization of both samples decreases in the existence range of the $D0_3$ phase with an increase in temperature up to 400–450 °C. Above $T_S \approx 400$ °C (Fig. 7a), a growth of the ferromagnetic $L1_2$ phase leads to an increase of sample's magnetization. The highest rate of this phase transition at instant heating is around 500 °C (T_m) according to the derivative curve. After reaching maximal magnetization at about 550 °C, M(T) slowly decreases with increasing temperature until 620–625 °C. At this temperature, the ferromagnetic $L1_2$ phase undergoes a transition to the non-ferromagnetic phases $D0_{19}$ and $D0_3$. If the heating and cooling cycle is repeated several times (Fig. 7b), the magnetization of the sample at room temperature increases due to the remaining $L1_2$ phase (see section 3.3), while an increase in magnetostriction during heating starts at a lower temperature due to the easier growth of already existing grains with $L1_2$ structure.

3.2.4. *Internal friction*

Temperature dependent internal friction curves during heating

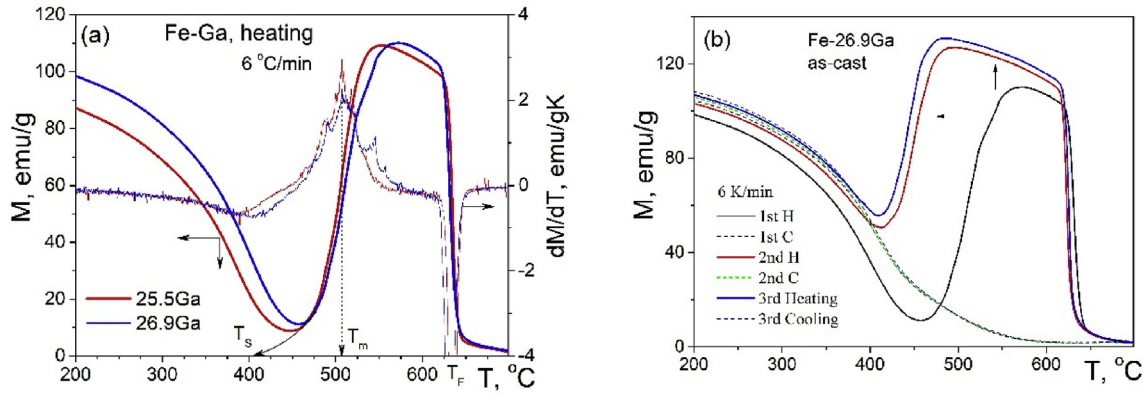

Fig. 7. Temperature dependence of the magnetization and its first derivation for Fe-25.5Ga and Fe-26.9Ga samples at heating (a), and magnetization in three subsequent heating and cooling runs for the Fe-26.9Ga sample (b).

and cooling of Fe-26.9Ga as-cast alloy are presented in Fig. 8. Similar results for the Fe-25.5Ga alloy were recently published in Ref. [31]. In the same reference, the nature of a thermally activated anelastic effect at 300–400 °C (depending on the measuring frequency) was discussed in terms of the Zener effect [32], i.e. in terms of stress-induced re-orientation of Ga–Ga pairs in the Fe–Ga solid solution. The $D0_3$ to $L1_2$ transition leads to the formation of a transient internal friction effect (P_{Tr}) which starts (T_S) from about 400 °C and has the highest transformation rate at 485 °C (T_m). The P_{Tr} peak is accompanied by an increase in Young's modulus, which is presented in Fig. 8 in arbitrary units.

3.2.5. Dilatometry

The thermal expansion of the alloy Fe-25.5Ga is shown in Fig. 9a. The slope of the expansion is almost constant until the temperature T_S (=460 °C) is reached, where the transition from a $D0_3$ phase to an $L1_2$ phase causes, an increase in slope. The $D0_3$ phase is a BCC derivative structure and the $L1_2$ phase is an FCC derivative structure; thus, their respective packing densities are around 68% and 74%, and therefore one could expect the opposite effect.

An explanation is given by this alloy's change of magnetization during the phase transition. As discussed earlier with the magnetization curves in section 3.2.3, the phase transition between the $D0_3$ and $L1_2$ phases are accompanied by a sharp increase in the magnetization. Thus, despite the difference of the packing densities, it is the transition from a paramagnetic phase to a ferromagnetic phase which causes the increase of the thermal expansion.

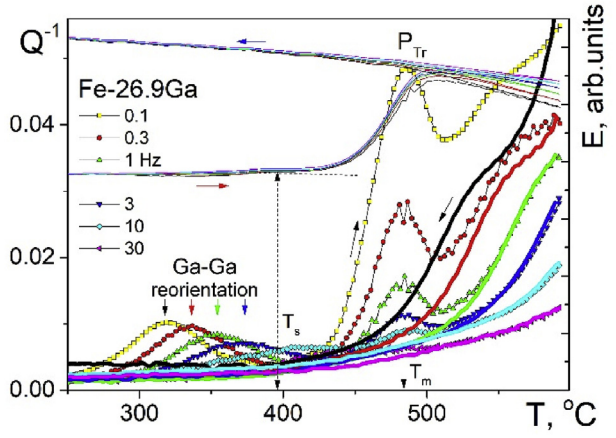

Fig. 8. Temperature dependent internal friction and Young's modulus for the as-cast Fe-26.9Ga alloy.

3.2.6. Differential scanning calorimetry

The dependences of the heat flow for three different heating rates (namely 5, 10, and 20 °C/min) are presented in Fig. 10. The exothermic reaction corresponding to the phase transition from $D0_3$ to the $L1_2$ phase shifts to lower temperatures by decreasing the heating rate (565, 545 and 515 °C at heating rates of 20, 10 and 5 °C/min, respectively). This is true also for other reactions. Approximations for all three transitions (from $D0_3$ to $L1_2$, from $L1_2$ to $D0_{19}$, and from $D0_{19}$ to B2) to 'zero heating rate' gives the following temperatures: the $D0_3$ to $L1_2$ transition starts at 458 °C and ends at 540 °C. It reaches a maximum of the transition rate at 506 °C. For the $L1_2$ to $D0_{19}$ transition, the maximum rate occurs at 633 °C; for the $D0_{19}$ to B2 transition the maximum occurs at 698 °C. These temperatures are collected in Table 3 in the column "0 °C/min".

All used techniques have demonstrated sensitivity to phase transitions in Fe–Ga alloys. Technical limitations for DMA concerning the maximum temperature allow the analysis of only the $D0_3$ to $L1_2$ transition. Table 2 summarizes the parameters of this transition in Fe-27Ga – the beginning, the end of the transition and the temperature of the maximal rate of the transition as recorded by all methods. The methods used are given in the order of increasing heating rate. ND and DSC tests were carried out for several heating rates.

3.3. Phase transitions during cooling

In situ neutron diffraction gives a general picture of non-equilibrium phase transitions during cooling. For a cooling rate of 2 °C/min, the following transitions take place (Fig. 11):

- **in Fe-25.5Ga:** A2 → (B2 →) $D0_3$ → $L1_2$ + 1% ($D0_{19}$ + A2),
- **in Fe-26.9Ga:** A2 → B2 → ($D0_{19}$ + $L1_2$), as it can be seen in Fig. 4.

It should be mentioned that an increase of the cooling rate to 8 °C/min leads to the appearance of some amount of A2($D0_3$) phase with increasing volume fraction.

The small difference between these two alloys is that in the Fe-25.5Ga alloy the volume fraction of the $L1_2$ phase after cooling with 2 °C/min is about 99%, while in the Fe-26.9Ga alloy after cooling the ratio of $L1_2$/$D0_{19}$ is about 1/2. Phase transition temperatures are collected in Table 3.

During cooling, the phase transition shifts to lower temperatures; for example, the transition B2→$D0_{19}$ takes place at a lower

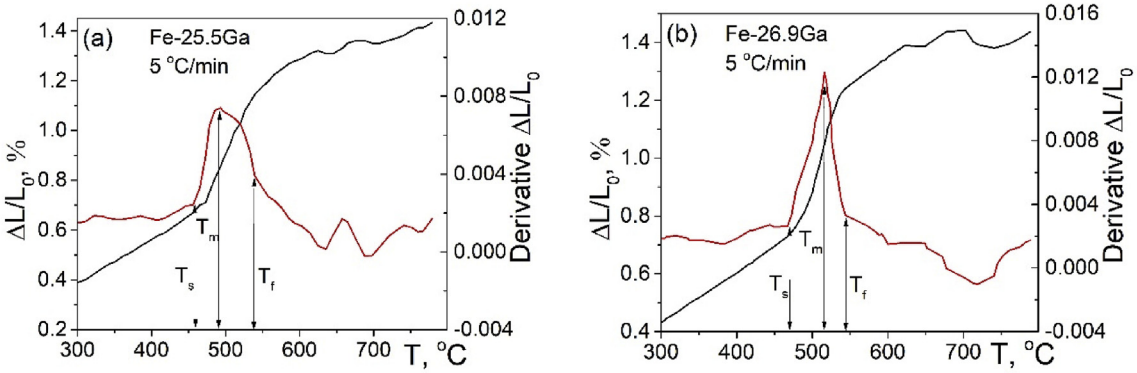

Fig. 9. Dilatometric test for Fe-25.5Ga (a) and Fe-26.9Ga (b) alloys.

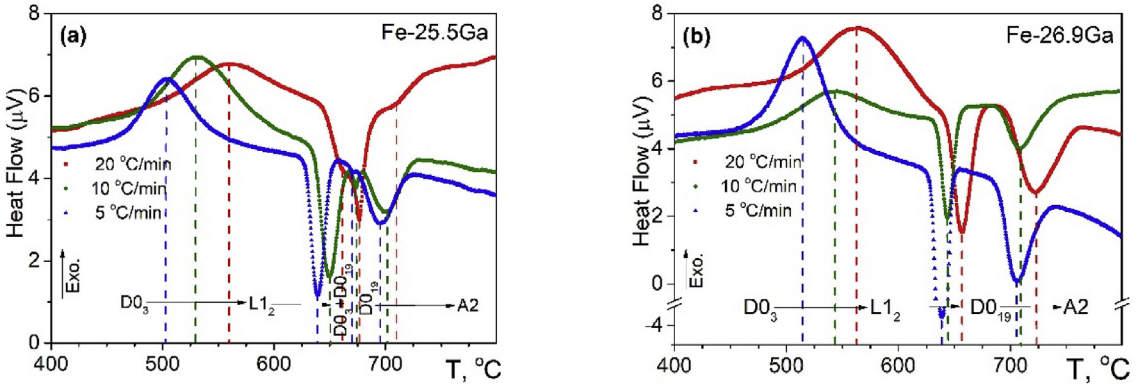

Fig. 10. Heat flow for as-cast Fe-25.5Ga (a) and Fe-26.9Ga (b) alloys at different heating rates (5, 10, 20 °C/min).

Table 2
Temperatures of beginning, end and most intensive $D0_3$ to $L1_2$ transition during heating according to different measuring techniques for alloy Fe-27Ga.

	RM	ND	TDIF	DT	VSM	DSC			
Heating rate, °C/min	1	2	2	5	6	0 (appr)	5	10	20
	The $D0_3$ to $L1_2$ transition								
Start of transition T_s, °C	430	425	425	468	410	458	465	480	495
Maximal rate T_m, °C	462	440	485	514	505	506	515	545	565
Finish of transition T_f, °C	485	465	505	544	550	540	560	590	630
	The $L1_2$ to $D0_{19}$ transition								
Start of transition T_s, °C	615	600	–		617	617	622	630	640
Maximal rate T_m, °C	624	610	–		631	633	639	644	657
Finish of transition T_f, °C	628	625	–		651	645	655	660	681
	The $D0_{19}$ to B2/A2 transition								
Start of transition T_s, °C		665	–			680	683	686	693
Maximal rate T_m, °C	693	685	–			699	706	707	722
Finish of transition T_f, °C		715	–			732	738	747	760

*DSC data approximation to zero heating rate.

temperature (650 °C at the cooling rate 5 °C/min) as compared to the reversed transition during heating (706 °C at the heating rate of 5 °C/min). By decreasing the cooling rate, the temperature corresponding to the phase transition increases (Fig. 12). The transition $D0_{19} \rightarrow L1_2$ takes place when reaching 505, 515 and 535 °C at cooling rates of 20, 10 and 5 °C/min, respectively.

Resistivity and VSM results during cooling are shown for the resistivity in Fig. 6 and for magnetometry in Fig. 7 (a and b), both together with data obtained during heating. For the resistivity measurements, a sample was heated up to 1000 °C and immediately cooled at the same rate of 1 °C/min. A cooling curve change of slope is observed at 674 °C, indicating a phase transition. The curve passes continuously from a maximum to a nearly linear curve until room temperature. Naturally, at cooling there is no phase transition around 462 °C, as the transition at this temperature during heating corresponds to the transition from the metastable $D0_3$ phase in as-cast samples to the equilibrium $L1_2$ phase. Phase transition may also depend on the highest temperature reached.

Variations in cooling rate from 1 to 2000 °C/min and analysis of

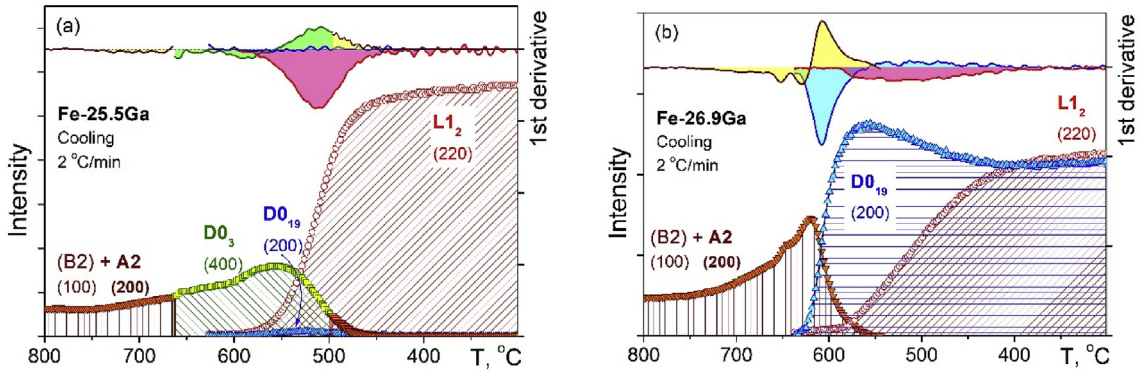

Fig. 11. Temperature dependencies of different phases of the fundamental diffraction peaks during a transition from initial (A2 phase) to final $L1_2$ phase state of the alloy Fe-25.5Ga (a), and to the $L1_2$+$D0_{19}$ phases state of the alloy Fe-26.9Ga (b) during cooling.

Table 3
Temperatures of onset, end and most intensive A2 to ($D0_{19}$ + $L1_2$) transition during cooling according to different measuring techniques for alloy Fe-27Ga.

	RM	ND	DT		DSC		
Heating rate, °C/min	1	2	5	0[a] (appr)	5	10	20
Start T_s, °C	674	640	650	593	592	570	568
Maximum T_m, °C	580	605	550	534	535	515	505
Finish T_f, °C	460	550	500	488	475	440	415

[a] DSC data approximation to zero cooling rate.

diffraction patterns of the samples allowed us to determine the 1st and the 2nd critical cooling rates: the 1st one is defined as the cooling rate of beginning of the appearance of the equilibrium $L1_2$ phase out from the metastable $D0_3$ phase and the 2nd one is the cooling rate at which no metastable phase (A2, B2 or $D0_3$) is recorded in the sample structure at RT. These results are discussed in the paper [33].

3.4. Impact of isothermal heat treatments

3.4.1. Microstructure characterization by SEM-EBSD, TEM, XRD

The sample microstructure and hardness were studied after long-term annealing for 300 h at different temperatures. Obviously, the 300 h annealing provokes a transition from metastable to equilibrium phases at lower temperatures as compared with instant heating. No phase transition was detected at annealing temperatures below 300 °C. With an increase in annealing temperature, one can see nucleation (Fig. 13a) on grain boundaries of the $D0_3$ grains and growth (Fig. 13b) of the $L1_2$ phase (red color on EBSD images, Fig. 13). After annealing at 500 °C (Fig. 13c) shows the transition is complete, and about 90% of the $L1_2$ phase is observed in the structure in agreement with the lever rule. Increase of the annealing temperature between 500 and 575 °C (both at 300 h) did not lead to pronounced changes in the $L1_2$ phase microstructure with an average grain size of 14 μm. The colors in Fig. 13d are the Euler colors and it is to demonstrate much smaller grains in the $L1_2$ phase as compared with the as cast alloy having a $D0_3$ structure.

These SEM-EBSD structural results are in agreement with the XRD study of the same samples (Fig. 14). After annealing at 300 °C, about 97% of the volume is in the $D0_3$ phase and 3% - belongs to the $L1_2$ phase. In contrast with neutron diffraction, there are no visible $D0_3$ superstructural reflections in XRD spectra, as the XRD contrast is 2.3 times smaller than in neutron diffraction spectra of Fe—Ga alloys. Similarly, to Ref. [34], the splitting of the A2 phase peaks in two components can be recorded especially in those with high 2θ values (Fig. 14a for Fe-25.5Ga and Fig. 14b for Fe-26.9Ga). The phase transition from a metastable to the stable $L1_2$ phase is approximately completed between 400 and 450 °C.

As similar results were obtained from both bulk and powder samples, we can conclude from the peak intensities that the volume fraction of the $L1_2$ phase in Fe-25.5Ga and Fe-26.9Ga after annealing at 300 °C amount to about 3% and 10%; respectively, after annealing at 400 °C this value amount to 78% and 89%. Annealing at higher temperatures leads to 100% $L1_2$ structure not only in the Fe-26.9Ga alloy but also in the Fe-25.5Ga alloy in agreement with in situ neutron diffraction results (Fig. 4) but in contrast with the equilibrium phase diagram [19–21]. Chemical compositions of the

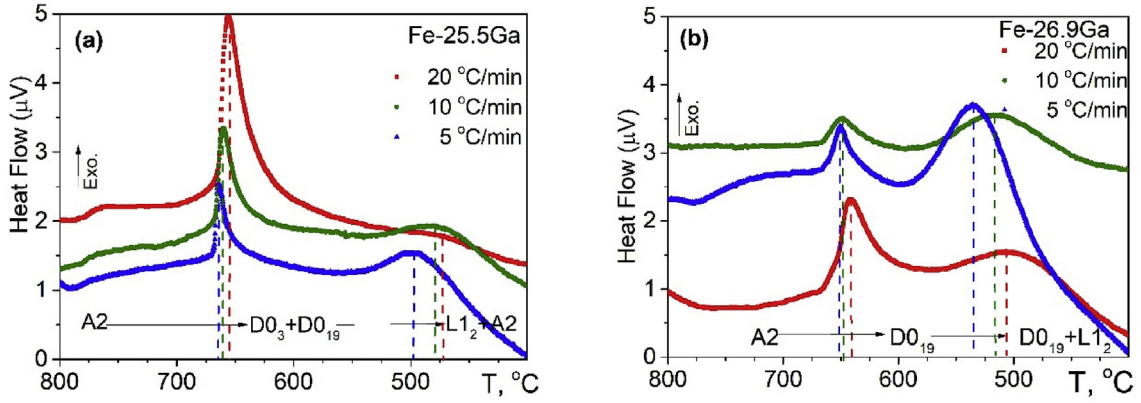

Fig. 12. Heat flow for the as-cast Fe-25.5Ga (a) and Fe-26.9Ga (b) alloys at different cooling rates (5, 10, 20 °C/min).

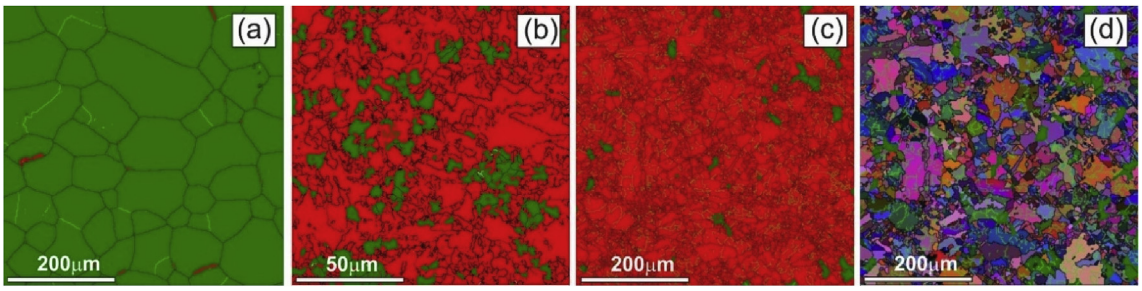

Fig. 13. SEM-EBSD structures of Fe-25.5Ga samples annealed for 300 h at 300 °C (a), 350 °C (b) and 500 °C (c, d). In the figures a–c (EBSD), the green color is reserved for BCC-originated (A2, $D0_3$) phases and the red color for $L1_2$ phase. The same colors are also used in Fig. 1 to indicate the phase ratios. (For interpretation of the references to color in this figure legend, the reader is referred to the Web version of this article.)

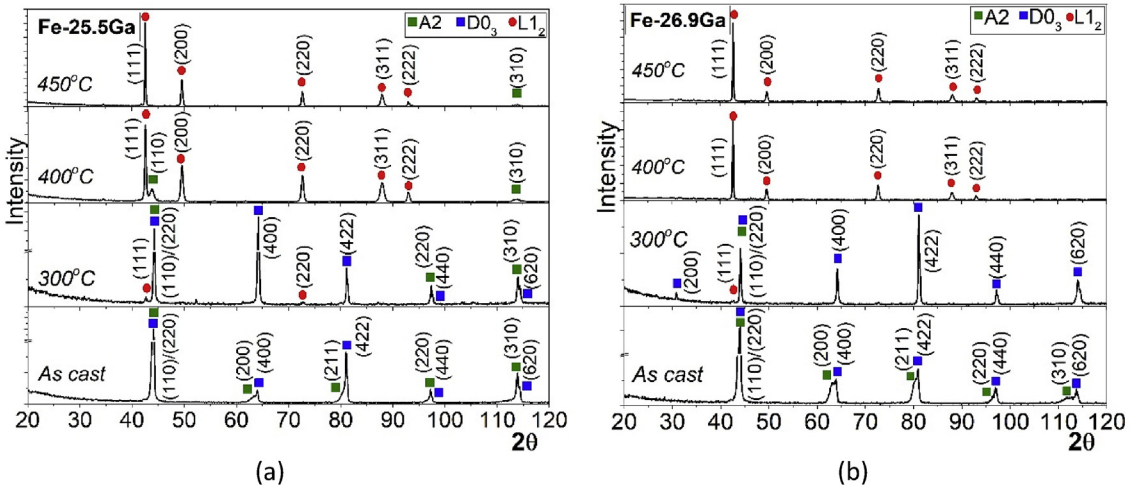

Fig. 14. X-ray diffraction patterns for Fe-25.5Ga (a) and Fe-26.9Ga (b) alloys.

samples checked by EDS as well as XRD spectra were checked several times to avoid artefacts.

Fig. 15 shows the microstructure of $D0_3$ and $L1_2$ phases in an Fe-26.9Ga type sample after 10 h annealing at 400 °C. The phases within the sample were identified using EBSD (not shown) and electron transparent TEM specimen were prepared from the characteristic regions. Fig. 15a shows the structure of the $D0_3$ phase and the corresponding SAED pattern that was recorded with the electron beam direction along the [001] axis of $D0_3$. The appearance of the forbidden reflections in electron diffraction pattern is due to small chemical variations in the $D0_3$ phase. Our preliminary energy dispersive X-ray measurements in the TEM suggest a formation of a Ga-rich regions. Fig. 15b shows the microstructure of the $L1_2$ phase, which typically contains a large density of planar defects and grain boundaries. The corresponding electron diffraction pattern confirms the $L1_2$ structure. The appearance of the satellite reflections is due to the overlapping of two $L1_2$ grains in the electron beam direction. In general, the TEM studies reveal the large single crystalline $D0_3$ grains formation with low defect density, but a chemical variation. In contrast the $L1_2$ phase contains high density grain boundaries and is characterized by a presence of many planar defects. The details of the structure, chemical variations and the corresponding magnetic structure in $D0_3$ and $L1_2$ phases measured by TEM is a subject of a different manuscript.

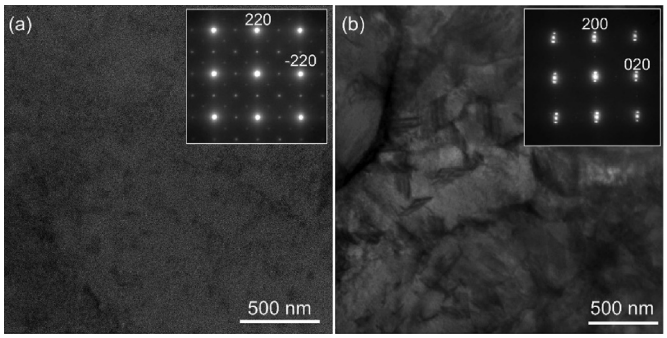

Fig. 15. BF TEM images of the microstructure of $D0_3$ (a) and $L1_2$ phases (b) in an Fe-26.9Ga sample. Insets are the electron diffraction patterns recorded along the [001] direction of the corresponding regions.

3.4.2. Microhardness measurements

Annealing of as-cast samples leads to a sample hardness increase (Fig. 16). A small HV increase after annealing at 300 °C is, most probably, the result of additional $D0_3$ sample structure ordering. This hypothesis is confirmed by results of Mössbauer spectroscopy results.

A significant hardness increases after annealing at 400 °C is due to intensive $L1_2$ phase structure growth. Finally, a moderate hardness decreases after annealing at 500 °C can most probably be assigned to stress relaxation, which was detected in a two-phase $D0_3 + L1_2$ structure in Ref. [35].

3.4.3. Mössbauer measurements

The Mössbauer spectra of an as-cast sample (a) and a sample

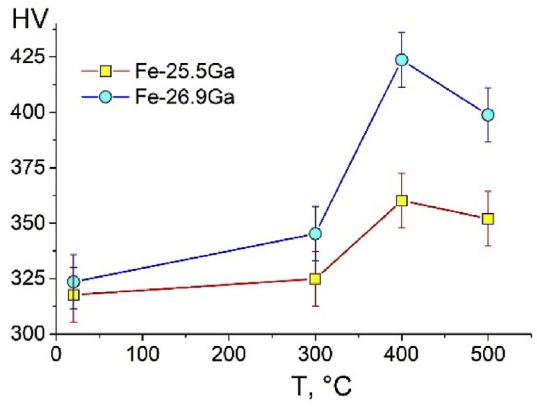

Fig. 16. Vickers hardness dependence on the annealing temperature for Fe-25.5Ga and Fe-26.9Ga alloys.

that has been additionally annealed at 300 °C(b) are shown in Fig. 17. The spectrum recorded for the as-cast sample was decomposed into six sextets providing the minimum value of χ^2, and that for the sample additionally annealed at 300°C for 5 h was decomposed into four sextets, also with a minimum value of χ^2. The obtained parameters of the spectra are listed in Table 4. According to this summarized analysis, all six sextets in the spectrum of the as-cast sample are explained by the appearance of Fe atoms at non-equivalent positions in the nearest coordination sphere. The Mössbauer spectroscopy of the sample annealed at 300 °C shows that atomic ordering takes place during annealing. The first sextet refers to atoms with a coordination number of 8, in whose environment Ga atoms are absent. The weak sextets 2 and 3 stem from

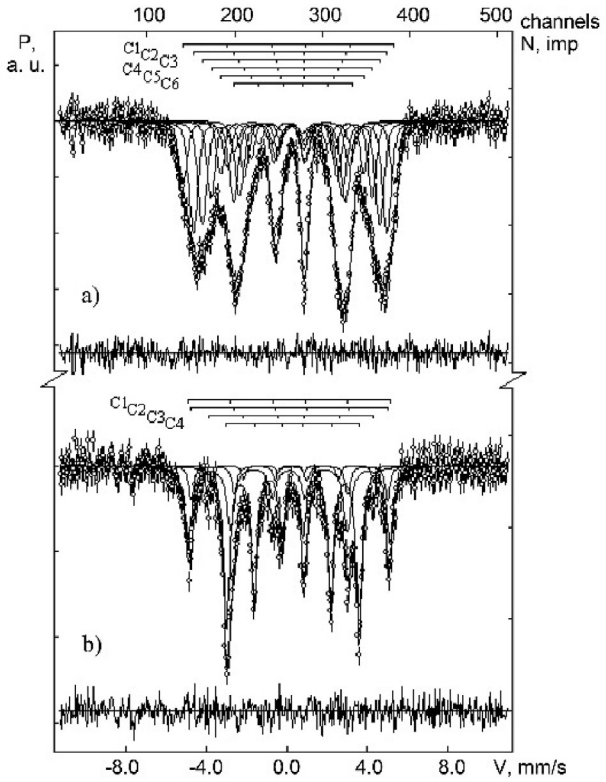

Fig. 17. Room-temperature ^{57}Co Mössbauer spectra of the Fe-26.9Ga alloy samples: in as-cast state (a) and in the annealed at 300 °C, 5 h state (b).

Fe atoms that are surrounded by 1 and 2 Ga atoms, respectively, and sextet 4 originates from configurations where Fe atoms are surrounded by 4 Ga atoms. The sextets 2 and 3 with areas of 3 and 3.2% respectively, indicate that 100% ordering does not occur, but the degree of ordering of the alloy after annealing is quite high.

3.4.4. Magnetostriction

The magnetostriction of metastable $D0_3$ and equilibrium $L1_2$ phases has the opposite sign: positive for metastable $D0_3$ and negative for the equilibrium phase $L1_2$ (Fig. 18). The saturation magnetostriction for the as-cast state with $D0_3$ structure is positive (100 ppm), whereas it is negative (−49 ppm) after annealing, since the material consists mainly of the $L1_2$ phase [30]. Formation of the two-phase structure consisting of metastable $D0_3$ and the equilibrium $L1_2$ phases leads to an interesting dependence of the magnetostriction on the magnetic field, as discussed in Refs. [35,36].

3.4.5. MFM measurements

The magnetic topology for such a two-phase structure in a Fe-27Ga alloy is presented in Fig. 19. The magnetic domain structure for $D0_3$ and $L1_2$ phases are rather different (Fig. 19b): the $L1_2$ phase contains random and irregular magnetic domains whereas the $D0_3$ phase has plate-like magnetic domains with a distinct magnetic substructure.

3.4.6. Low-temperature heat capacity

Low temperature heat capacity, c_p, was measured for the Fe-27Ga alloy in different states induced by selected heat treatment procedures. The results are summarized in Fig. 20a.

At low temperatures, typically between 5 and 10 K, the heat capacity can be presented as a sum of a linear and a T^3 term corresponding to the electronic and Debye contributions (see Ref. [37] for further discussion of all contributions):

$$c_p(T) = c_p^e(T) + c_p^D(T) = \gamma T + \beta T^3 = \gamma T + \frac{12\pi^4}{5} R \left(\frac{T}{\Theta}\right)^3 \quad (1)$$

The parameter β is directly related to the Debye temperature Θ, $\beta = \frac{12\pi^4}{5} R \left(\frac{1}{\Theta}\right)^3$. We fitted the measured c_p values for different datasets between 5 and 10 K using Eq. (1) and the determined parameters are given in Table 1. Using the value of Θ from this low-temperature fit, the Debye-type phonon heat capacity, $c_p^D(T)$, in the whole temperature interval was determined as the corresponding Bloch-Grüneisen integral. Then, we determined the excess heat capacity with respect to the sum of the linear and Debye-type terms as $c_p^{BP}(T) = c_p(T) - c_p^e(T) - c_p^D(T)$. Such a contribution is known as Boson peak in the literature on heat capacity of amorphous materials [38,39] and it is plotted in Fig. 20b.

The determination of the excess contribution is a delicate task and a note is due here. One may use the Bloch-Grüneisen integral (in addition to a linear term) to fit the experimentally determined heat capacity in the whole temperature interval from 2 K to 100 K. However, the excess contributions to the Debye-type heat capacity – if they are present – would affect such a fit. Typically, one expects the excess contributions between 12 K and 50 K [37,38] which would correspond to excess localized modes in phonon spectra. Therefore, we have used a different approach as described in the paper, see above, by fitting the experimental data between 5 K and 10 K where the Debye model is assumed to be appropriate.

The inset in Fig. 20b shows the excess heat capacity in the coordinates of c_p^{BP}/T^3 vs. T. This type of presentation is used in the metallic glass community and it highlights the excess contributions of low-frequency (about THz) atomic vibrations. If electronic and Debye-type contributions to the heat capacity would solely be

Table 4
Mössbauer parameters of the Fe-26.9Ga alloy samples: in the as-cast state and in the annealed at 300 °C, 5 h state.

Sample Fe—Ga	Spectrum component	Isomeric shift δ, mm/s	Quadrupole splitting Δ, mm/s	Magnetic fields on the nuclei Fe^{57} H, kOe	Area of component S,%	The width of the resonance line is G, mm/s
Fe-26.9Ga in as-cast state	C1	0.08	0.02	325.9	15.4	0.52
	C2	0.14	0.04	297.6	**27.0**	0.53
	C3	0.20	0.02	272.5	**24.3**	0.53
	C4	0.22	0.04	247.5	16.0	0.47
	C5	0.27	0.00	220.2	10.1	0.44
	C6	0.31	0.01	182.3	7.2	0.53
Fe-26.9Ga in annealed at 300 °C, 5 h state	C1	0.12	−0.01	327.6	36.0	0.38
	C2	0.18	0.04	309.3	**3.0**	0.22
	C3	0.21	0.01	288.1	**3.2**	0.21
	C4	0.28	0.00	253.9	57.8	0.36

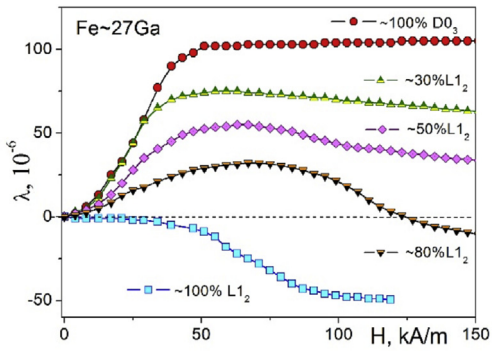

Fig. 18. Magnetostriction for the Fe-27Ga type alloy in different states: as-cast (100% $D0_3$ phase) and with different amounts of $L1_2$ phase produced by isothermal annealing (adapted from Refs. [30,36]).

expected, the value of c_p^{BP} would be equal to zero in view of Eq. (1).

However, there is a systematic deviation of the c_p^{BP} values from zero in the Fe—Ga alloy with two prominent features. First, both positive and negative deviations are seen at $T \geq 25$ K for different sets. Second, a local maximum in the c_p^{BP}/T^3 curve might be indicated for some curves at about 20 K if the Debye-type contribution is subtracted.

The type of the excess contributions, i.e. with respect to the Debye-type heat capacity, turned out to depend on the lattice type. In its as-quenched state (the fraction of the $L1_2$ phase is almost zero) the low-temperature approximation in Eq. (1) overestimates the density of low-energy vibrations and correspondingly the estimated Debye temperature is lowest, Table 5. As a result, systematic negative deviations from the anticipated Debye-type heat capacities are seen. The applied annealing treatments induced a lattice transformation to the FCC-derivative $L1_2$ structure, and the Debye model works better. As soon as the fraction of $L1_2$ phase approaches almost 100%, the low-temperature approximation describes almost perfectly the resulting cp up to 100 K. One may note a systematic trend in the Debye temperatures as a result of annealing treatments which promote the formation of the $L1_2$ phase.

4. Conclusions

Two as-cast Fe—Ga alloys with structures close to the stoichiometric A_3B composition (25.5 and 26.9 at.% Ga) were studied during heating and cooling with different rates, including long-term annealing (up to 300 h) by neutron diffraction, XRD, DSC, VSM, dilatometry, internal friction, HV, SEM and TEM to make the following conclusions:

1) Careful study of long-term annealed Fe-25.5Ga alloy suggests that the boundary between the single ($L1_2$) and two-phase ranges ($L1_2$ + A2) of the equilibrium phase diagram (placed at about 26.4%Ga in diagrams [19—21]) should be shifted to smaller Ga concentrations (proposed in Fig. 1 by the blue dotted line). A more detailed study of this effect is ongoing and will be published elsewhere.
2) As-cast samples of the studied compositions definitely include the $D0_3$ phase in agreement with the sketch-diagram proposed by Okamoto [40] but they do not include the A2 phase as proposed by the equilibrium phase diagram [19—21]. A more

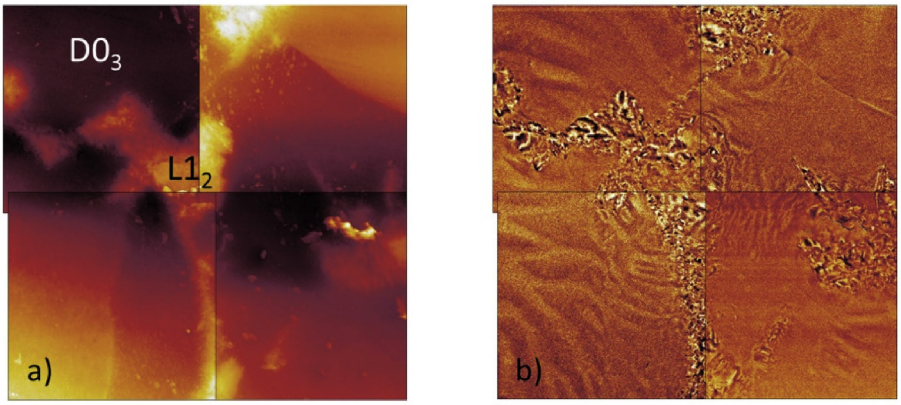

Fig. 19. Stitched micrograph to extend the maximum imaging size from 45 × 45 μm to about 80 × 80 μm: topography (a) and MFM (b) images in the two-phase ($D0_3$ + $L1_2$). structure.

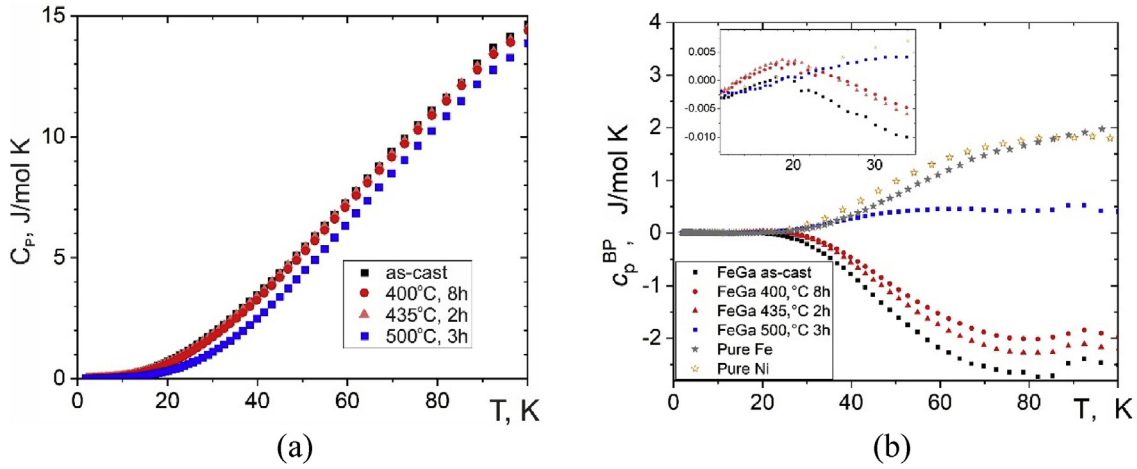

Fig. 20. Low-temperature heat capacity of the Fe-26.9Ga alloy in as-quenched state and after different heat treatments (a) and the extracted excess contribution to the Debye-type heat capacity (b). The inset in (b) replots the excess heat capacity, i.e. the Boson peak c_p^{BP}, in the coordinates c_p^{BP}/T^3 vs T.

Table 5
Fit parameters according to Eq. (1) for the measured heat capacities of the Fe-26.9Ga alloys in different states approached by annealing at the given temperatures for the given times.

State	fraction of $L1_2$	γ (mJ/mol·K^2)	Θ (K)
As-cast	0%	6.654	301
400 °C, 8 h	32%	4.768	316
435 °C, 2 h	28%	5.697	309
500 °C, 3 h	~100%	1.668	381

detailed TEM study of the nano-sized $D0_3$ domain structure of the alloys is discussed in Ref. [41].

3) The following phase transitions take place in both studied alloys during heating with the rate of 2 °C/min to 850 °C, i.e. to the A2 range of the equilibrium phase diagram: $D0_3 \rightarrow L1_2 \rightarrow D0_{19} \rightarrow B2 \rightarrow A2$

The temperature ranges of the phase transitions from metastable $D0_3$ to the equilibrium $L1_2$ phase were recorded for different heating rates by different 'in situ' methods (ND, DSC, VSM, dilatometry, IF) and are collected in Table 2. These data are consistent between the different methods. The low-temperature heat capacity measurements reveal a systematic excess contributions variation with respect to the Debye-type model in the Fe-27Ga alloys from a depleted density of states with frequencies of about 1 THz to an enhanced density when the as-quenched $D0_3$ phase is transformed to the $L1_2$ phase.

4) If long-term annealing (300 h) of as-cast samples at 300–500 °C is applied, the transition from the metastable structure to the equilibrium phases starts at lower temperatures. In contrast to the Fe-26.9Ga alloy, whose equilibrium structure is well predicted by the phase diagram [19–21], the composition Fe-25.5Ga exhibits nearly 100% $L1_2$ structure after annealing at 450–575 °C. This suggests the necessity to correct the phase diagram.
5) Phase transitions during cooling play an important role as they form the final structure of the alloys. For cooling of the studied alloys from the A2 range with a rate of 2 °C/min the following reactions take place:
- in Fe-25.5Ga: $A2 \rightarrow (B2 \rightarrow) D0_3 \rightarrow L1_2 + 1\%\ (D0_{19} + A2)$,
- in Fe-26.9Ga: $A2 \rightarrow 2/3D0_{19} + 1/3L1_2$.

Variation of the cooling rate from 1 to 8 °C/min for in situ neutron diffraction tests of the Fe-26.9Ga alloy demonstrates that an increase in cooling rate leads to the appearance of the A2 phase in the sample structure.

Acknowledgements

The work was carried out with support from the Ministry of Education and Science of the Russian Federation in the framework of Increase Competitiveness Program of NUST "MISIS", implemented by a governmental decree dated 16th of March 2013, No 211 and RNF project no. 19-72-20080. Authors are very grateful to their colleagues for their valuable help and fruitful discussions: T.B. Sagalova (XRD), E.N. Zanaeva (VSM), J. Cifre (IF), A.Yu. Churyumov (sample producing), and V. Kulitskii (sample treatment) and J. Campbell for fruitful discussions. I.S.G. is grateful for DAAD grant Personal ref. no.: 91573930 (2018).

References

[1] R.A. Kellogg, Development and Modeling of Iron–Gallium Alloys, PhD Thesis Engineering Mechanics, Iowa State University, Ames, Iowa, 2003.
[2] T.V. Jayaraman, N. Srisukhumbowornchai, S. Guruswamy, M.L. Free, Corrosion studies of single crystals of iron–gallium alloys in aqueous environments, Corros. Sci. 49 (2007) 4015–4027. https://doi:10.1016/j.corsci.2007.05.010.
[3] H. Wang, Y. Zheng, J. Liu, C. Jiang, Y. Li, In vitro corrosion properties and cytocompatibility of Fe-Ga alloys as potential biodegradable metallic materials, Mater. Sci. Eng. C 71 (2017) 60–66. https://doi:10.1016/j.msec.2016.09.086.
[4] J. Atulasimha, A.B. Flatau, E. Summers, Characterization and energy-based model of the magnetomechanical behavior of polycrystalline iron–gallium alloys, Smart Mater. Struct. 16 (2007) 1265–1276. https://doi:10.1088/0964-1726/16/4/039.
[5] J.M.D. Coey, Magnetism and Magnetic Materials, Cambridge University Press, New York, 2010.
[6] A.E. Clark, Ferromagnetic materials, in: E.P. Wohlfarth (Ed.), Magnetostrictive Rare Earth-Fe2 Compounds, North-Holland Publishing Company, Amsterdam, 1980, pp. 531–589.
[7] H. Wang, Y.N. Zhang, T. Yang, Z.D. Zhang, L.Z. Sun, R.Q. Wu, Ab initio studies of the effect of nanoclusters on magnetostriction of Fe_{1-X} Ga_X alloys, Appl. Phys. Lett. 97 (2010) 1–4. https://doi:org/10.1063/1.3533659.
[8] E.M. Summers, T.A. Lograsso, M. Wun-Fogle, Magnetostriction of binary and ternary Fe–Ga alloys, J. Mater. Sci. 42 (2007) 9582–9594. https://doi:10.1007/s10853-007-2096-6.
[9] H.D. Chopra, M. Wuttig, Non-joulian magnetostriction, Nature 521 (2015) 340–351. https://doi:10.1038/nature14459.
[10] A.E. Clark, J.B. Restorff, M. Wun-Fogle, T.A. Lograsso, D.L. Schlagel, Magnetostrictive properties of body-centered cubic Fe-Ga and Fe-Ga-Al alloys, IEEE Trans. Magn. 36 (2000) 3238–3240.
[11] J.B. Restorff, M. Wun-Fogle, K.B. Hathaway, A.E. Clark, T.A. Lograsso, G. Petculescu, Tetragonal magnetostriction and magnetoelastic coupling in Fe-

Al, Fe-Ga, Fe-Ge, Fe-Si, Fe-Ga-Al, and Fe-Ga-Ge alloys, J. Appl. Phys. 111 (023905) (2012) 1–12. https://doi:10.1063/1.3674318.
[12] A.E. Clark, M. Wun-Fogle, J.B. Restorff, T.A. Lograsso, G. Petculescu, Magnetostriction and elasticity of body centered cubic $Fe_{100-X}Be_X$ alloys, J. Appl. Phys. 95 (2004) 6942–6944. https://doi:10.1063/1.1688676.
[13] P. Mungsantisuk, R.P. Corson, S. Guruswamy, Influence of Be and Al on the magnetostrictive behavior of FeGa alloys, J. Appl. Phys. 98 (123907) (2005) 1–6. https://doi:10.1063/1.2149491.
[14] J.B. Restorff, M. Wun-Fogle, A.E. Clark, T.A. Lograsso, A.R. Ross, D.L. Schlagel, Magnetostriction of ternary Fe–Ga–X alloys (X=Ni, Mo, Sn, Al), J. Appl. Phys. 91 (8225) (2002) 8225–8227. https://doi:10.1063/1.1452220.
[15] C. Bormio-Nunes, R.S. Turtelli, H. Mueller, R. Grössinger, H. Sassik, M.A. Tirelli, Magnetostriction and structural characterization of Fe–Ga–X (X = Co, Ni, Al) mold-cast bulk, J. Magn. Magn. Mater. 290–291 (2005) 820–822. https://doi:10.1016/j.jmmm.2004.11.372.
[16] A.E. Clark, J.B. Restorff, M. Wun-Fogle, K.B. Hathaway, T.A. Lograsso, M. Huang, E. Summers, Magnetostriction of ternary Fe-Ga-X (X=C, V, Cr, Mn, Co, Rh) alloys, J. Appl. Phys. 101 (09C507) (2007) 1–4. https://doi:10.1063/1.2670376.
[17] J.H. Li, X.X. Gao, J. Zhu, X.Q. Bao, T. Xia, M.C. Zhang, Ductility, texture and large magnetostriction of Fe–Ga-based sheets, Scr. Mater. 63 (2010) 246–249. https://doi:10.1016/j.scriptamat.2010.03.068.
[18] M.V. Matyunina, M.A. Zagrebin, V.V. Sokolovskiy, O.O. Pavlukhina, V.D. Buchelnikov, A.M. Balagurov, I.S. Golovin, Phase diagram of magnetostrictive Fe-Ga alloys: insights from theory and experiment, Phase Transitions 92 (2) (2019) 101–116. https://doi:10.1080/01411594.2018.1556268.
[19] W. Köster, T. Gödecke, Über den Aufbau des Systems Eisen-Gallium zwischen 10 und 50 At.-% Ga und dessen Abhängigkeit von der Wärmebehandlung. I. Das Diagramm der raumzentrierten Phasen, Z. Metallkde, 1977.
[20] W. Köster, T. Gödecke, Über den Aufbau des Systems Eisen-Gallium zwischen 10 und 50 At.-% Ga und dessen Abhängigkeit von der Wärmebehandlung. II. Das Gleichgewichtsdiagramm, Z. Metallkde, 1977.
[21] W. Köster, T. Gödecke, Über den Aufbau des Systems Eisen-Gallium zwischen 10 und 50 At.-% Ga und dessen Abhängigkeit von der Wärmebehandlung. III. Ein Unterkühlungsdiagramm und Diagramme für die Vorgänge beim Anlassen ofengekühlter und abgeschreckter Legierungen. Z. Metallkde, 1977.
[22] O. Ikeda, R. Kainuma, I. Ohnuma, K. Fukamichi, K. Ishida, Phase equilibria and stability of ordered b.c.c. phases in the Fe-rich portion of the Fe–Ga system, J. Alloy. Comp. 347 (2002) 198–205. https://doi:10.1016/S0925-8388(02)00791-0.
[23] A.M. Balagurov, I.S. Golovin, I.A. Bobrikov, V.V. Palacheva, S.V. Sumnikov, V.B. Zlokazov, Comparative study of structural phase transitions in bulk and powdered Fe-27Ga alloy by real-time neutron thermodiffractometry, J. Appl. Crystallogr. 50 (2017) 198–210. https://doi:10.1107/S1600576716020045.
[24] L. Abadlia, F. Gasser, K. Khalouk, M. Mayoufi, J.G. Gasser, New experimental methodology, setup and Labview program for accurate absolute thermoelectric power and electrical resistivity measurements between 25 and 1600K: application to pure copper, platinum, tungsten and nickel at very high temperatures, Rev. Sci. Instrum. 85 (095121) (2014) 1–11. https://doi:10.1063/1.4896046.
[25] A. Messaoud, N. Fazel, L. Garoux, F. Gasser, R. Ben Younes, J.G. Gasser, A new high temperature design to determine electrical and thermal conductivities and thermoelectric power. Applications to the sintered composite AgNi (90/10) "pseudo-alloy", J. Alloy. Comp. 739 (2018) 407–417. https://doi:10.1016/j.jallcom.2017.12.140.
[26] I.S. Golovin, Anelasticity of Fe-Ga based alloys, Mater. Des. 88 (2015) 577–587. https://doi:10.1016/j.matdes.2015.08.160.
[27] J.S. Hwang, K.J. Lin, C. Tien, Measurement of heat capacity by fitting the whole temperature response of a heat-pulse calorimeter, Rev. Sci. Instrum. 68 (1997) 94–101. https://doi:10.1063/1.1147722.
[28] YuP. Mitrofanov, M. Peterlechner, I. Binkowski, M.Yu Zadorozhnyy, I.S. Golovin, S.V. Divinski, G. Wilde, The impact of elastic and plastic strain on relaxation and crystallization of Pd–Ni–P-based bulk metallic glasses, Acta Mater. 90 (2015) 318–329. https://doi:10.1016/j.actamat.2015.03.001.
[29] O. Kubaschewski, IRON—Binary Phase Diagrams, Springer Science, LLC, 1982, p. 41.
[30] I.S. Golovin, A.M. Balagurov, V.V. Palacheva, A. Emdadi, I.A. Bobrikov, V.V. Cheverikin, A.S. Prosviryakov, S. Jalilzadeh, From metastable to stable structure: the way to construct functionality in Fe-27Ga alloy, J. Alloy. Comp. 751 (2018) 364–369. https://doi:10.1016/j.jallcom.2018.04.127.
[31] I.S. Golovin, V.V. Palacheva, J. Cifre, C. Jiang, Internal friction in Fe-Ga alloys at elevated temperatures, J. Alloy. Comp. 785 (2019) 1257–1263, https://doi.org/10.1016/j.jallcom.2019.01.265.
[32] C. Zener, Elasticity and Anelasticity of Metals, University of Chicago Press, Chicago, Illinois, 1948.
[33] I.S. Golovin, A.M. Balagurov, I.A. Bobrikov, S.V. Sumnikov, Cooling Rate as a Tool of Tailoring Structure of Fe-(9-33%)Ga Alloys, (submitted to Intermetallics) (Under review).
[34] T.A. Lograsso, E.M. Summers, Detection and quantification of $D0_3$ chemical order in Fe–Ga alloys using high resolution X-ray diffraction, Mater. Sci. Eng. A 416 (2006) 240–245. https://doi:10.1016/j.msea.2005.10.035.
[35] V.V. Palacheva, A. Emdadi, F. Emeis, I.A. Bobrikov, A.M. Balagurov, S.V. Divinski, G. Wilde, I.S. Golovin, Phase transitions as a tool for tailoring magnetostriction in intrinsic Fe-Ga composites, Acta Mater. 130 (2017) 229–239. https://doi:10.1016/j.actamat.2017.03.049.
[36] I.S. Golovin, A.M. Balagurov, A. Emdadi, V.V. Palacheva, I.A. Bobrikov, V.V. Cheverikin, E.N. Zanaeva, D. Mari, Phase transitions in Fe-27Ga alloys: guidance to develop functionality, Intermetallics 100 (2018) 20–26. https://doi:10.1016/j.intermet.2018.05.016.
[37] A. Gupta, B. Tas Kavakbasi, B. Dutta, B. Grabowski, M. Peterlechner, T. Hickel, S.V. Divinski, G. Wilde, J. Neugebauer, Low temperature features in the heat capacity of unary metals and intermetallics for the example of bulk aluminum and Al_3Sc, Phys. Rev. B. 95 (094307) (2017) 1–10. https://doi:10.1103/PhysRevB.95.094307.
[38] T. Brink, L. Koch, K. Albe, Structural origins of the boson peak in metals: from high-entropy alloys to metallic glasses, Phys. Rev. B. 94 (224203) (2016) 1–9. https://doi:10.1103/PhysRevB.94.224203.
[39] Y.P. Mitrofanov, M. Peterlechner, S.V. Divinski, G. Wilde, Impact of plastic deformation and shear band formation on the boson heat capacity peak of a bulk metallic glass, Phys. Rev. Lett. 112 (135901) (2014) 1–5. https://doi:10.1103/PhysRevLett.112.135901.
[40] H. Okamoto, Phase Diagrams of Binary Iron Alloys, ASM International, Materials Park, OH, 1993, p. 147.
[41] Tingyan Jina, Hui Wang, Igor S. Golovin, Chengbao Jiang. Structure Investigation on Magnetostrictive $Fe_{100-x}Ga_x$ and $(Fe_{100-x}Ga_x)_{99.8}Tb_{0.2}$ Alloys for $19 \leq X \leq 29$.